Specific heat and NMR evidence for the low Fermi-level density of states in semimetallic ScSb

C. N. Kuo,[1,2] C. C. Chen,[1] C. M. Chang,[3] R. Y. Huang,[3] L. Y. Wang,[3] Y. K. Kuo,[3,*] and C. S. Lue[1,2,†]

[1]*Department of Physics, National Cheng Kung University, Tainan 70101, Taiwan*

[2]*Taiwan Consortium of Emergent Crystalline Materials, Ministry of Science and Technology, Taipei 10601, Taiwan*

[3]*Department of Physics, National Dong Hwa University, Hualien 97401, Taiwan*

(Received 2 February 2021; revised 9 June 2021; accepted 6 July 2021; published 19 July 2021)

We report the electronic and thermal properties of scandium monoantimonide ScSb by means of the Seebeck coefficient, thermal conductivity, specific heat, and nuclear magnetic resonance measurements. The experimental Seebeck coefficient exhibits a strong temperature dependence, and the theoretical calculation based on the two-band model provides a realistic description of the observed feature. The analysis of the thermal conductivity reveals that the lattice thermal conductivity dominates at low temperatures while electronic thermal conductivity makes a major contribution at high temperatures. A small value of the Sommerfeld coefficient of 0.38 mJ mol^{-1} K^{-2} was extracted from the low-temperature specific heat measurement, indicative of a low electronic Fermi-level density of states (DOS) in ScSb. Furthermore, we have deduced the Sc 3*d* and Sb 5*s* partial Fermi-level DOSs based on the Korringa behavior in the ^{45}Sc and ^{121}Sb NMR spin-lattice relaxation rates. The determined values of the DOS are quite low, giving strong evidence for the semimetallic character in ScSb.

DOI: 10.1103/PhysRevB.104.035135

I. INTRODUCTION

Monoantimonides *M*Sb (*M* = transition − metal and rare-earth metal elements) with the rocksalt-type structure have drawn attention due to the existence of the unusual transport behavior in the materials of this class [1–10]. One of the significant features is the presence of the extreme large magnetoresistance (XMR), which could be associated with the topological surface states and band inversion near the *X* point of the Brillouin zone [11]. LaSb, the well-studied system among the rare-earth monoantimonide series, has been reported to exhibit the XMR behavior with a quadratic field dependence [1,2]. Nevertheless, the observed quadratic XMR has been attributed to the nearly electron-hole compensation without topological origin since LaSb has been characterized as a topologically trivial semimetal, based on the theoretical and experimental evidence [1,2]. The titled compound ScSb, the first member of the monoantimonide family, receives less attention as compared to the isostructural LaSb, and its fundamental bulk properties remain unexplored. Previous studies of this material have been focused on the structural stability under external pressure [12–18]. Most of the recent investigations were theoretical work, mainly aimed at the topological state of nanolayers [19,20]. Very recently, the XMR signature was demonstrated in ScSb [7]. The MR obtained over a wide temperature range also obeys a nearly quadratic field dependence as B^n with $n = 1.94$, quite similar to that observed in LaSb. The electronic band structure calculation reveals the absence of a band inversion, indicative of a topologically trivial semimetal for ScSb. The scenario of the nearly electron-hole compensation accompanied by the mobility mismatch has thus been employed to understand the observed XMR behavior [7].

In order to gain more experimental insights into the semimetallic features of ScSb, we have carried out a combined study of single-crystalline ScSb by means of the electrical resistivity, Seebeck coefficient, thermal conductivity, specific heat, and nuclear magnetic resonance (NMR) measurements. Small Fermi-level density of states (DOS) has been extracted from the analyses of the low-temperature specific heat coefficient and NMR spin-lattice relaxation rates. These experimental results thus provide conclusive evidence for the conventional semimetallic nature in ScSb.

II. EXPERIMENT DETAILS

Single crystals of ScSb were grown by the Sb self-flux method. Sc pieces and Sb chunks with the starting composition Sc : Sb = 1 : 10 were placed in alumina crucibles, which were sealed in a silica glass tube under vacuum. The silica tube was placed into a furnace, heated to a dwell temperature of 1100 °C for 10 h, and then slowly cooled (3 °C/h) to 750 °C. Finally, the silica tube was inverted and centrifuged to separate the single crystals from excess Sb flux. A photograph of a selected crystal is shown in the inset of Fig. 1. The main panel of Fig. 1 shows the room-temperature single-crystal x-ray diffraction (XRD) pattern. All diffraction peaks can be indexed to the expected *Fm*3*m* structure with the lattice parameter $a = 5.814 \pm 0.005$ Å, close to those reported in the literature [7,12].

Electrical resistivity was measured using a standard four-probe method, with an electrical current flowing along the

*ykkuo@gms.ndhu.edu.tw
†cslue@mail.ncku.edu.tw

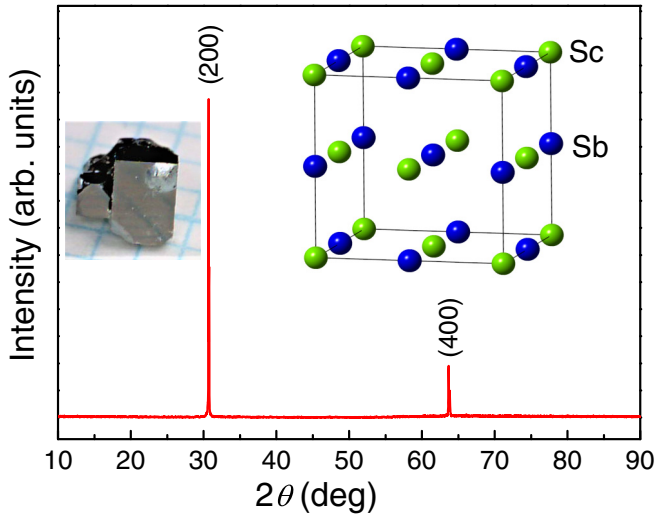

FIG. 1. Single-crystal x-ray diffraction of the (l00) planes measured at room temperature. The insets show a photograph of the single-crystalline ScSb and the corresponding crystal structure.

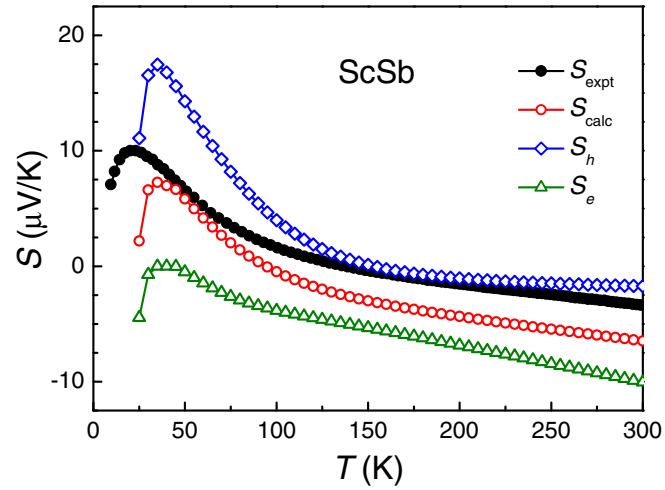

FIG. 2. Temperature dependence of the experimental and calculated total Seebeck coefficients of ScSb. The calculated partial Seebeck coefficients of holes (S_h) and electrons (S_e) as a function of temperature are displayed.

direction perpendicular to the (100) plane of the crystal. The data obtained from two batches of the crystal (sample 1 and sample 2) are displayed in the Supplemental Material [21] (also see Refs. [22–29]). The Seebeck coefficient and thermal conductivity measurements were performed in a closed-cycle refrigerator, using a direct heat-pulse technique. The temperature difference was detected by an E-type differential thermocouple with junctions thermally attached to two well-separated positions along the longest direction of the specimen. To obtain a higher accuracy for the thermal conductivity measurement, a large size of the ScSb crystal was used. The details of our thermoelectric techniques can be found in Ref. [29]. The low-temperature specific heat measurement was carried out in a Physical Property Measurement System (PPMS) with a heat-pulsed thermal relaxation calorimeter in the temperature range from 1.8 to 10 K, while the high-temperature specific heat measurement was performed in the temperature range from 85 to 300 K, using a high-resolution ac calorimeter.

Nuclear magnetic resonance measurements were performed on the powdered single crystals of ScSb under a constant field of 7.086 T. Both ^{45}Sc and ^{121}Sb NMR central transition line shapes were measured by spin-echo integration vs frequency. The NMR Knight shifts were determined from the position of the maximum of each spectrum relative to the corresponding reference frequency. The NMR spin-lattice relaxation rates were obtained by integrating the spin echo signal using the inversion recovery method.

The first-principles calculations for ScSb were performed based on density functional theory (DFT). The DFT calculations were performed using the generalized gradient approximation (GGA) with the Perdew-Burke-Ernzerhof (PBE) exchange-correlation (XC) functional [30] and the projector-augmented wave (PAW) method [31,32] as implemented in the Vienna *ab initio* simulation package (VASP) [33]. Self-consistent calculations, including the spin-orbit interaction, were performed with a 12 × 12 × 12 k-point mesh, and the lattice constant is kept at the experimental value (5.814 Å). Further computational details are presented in the Supplemental Material [21]; also see Refs. [22–28].

III. RESULTS AND DISCUSION

A. Thermoelectric measurements

The experimental Seebeck coefficient S_{expt} for ScSb is shown in Fig. 2. The strong temperature dependence indicates the multiband effect on the thermoelectric transport in ScSb. In order to substantiate our experimental perspectives, we have performed theoretical calculations for the Seebeck coefficients based on the electronic structures obtained by density functional theory (DFT) calculations. The details of the DFT calculations are given in the Supplemental Material [21]. For materials with a large band separation between the valence and conduction bands, the Seebeck coefficient of holes increases with increasing temperature when the Fermi level lies in the valence band (p type). In contrast, the Seebeck coefficient of electrons decreases with increasing temperature when the Fermi level lies in the conduction band (n type). For semimetals with slight band overlaps, the bipolar transport should be taken into account with two types of carriers. The total Seebeck coefficient can be described as $S_{\text{calc}} = (\sigma_h S_h + \sigma_e S_e)/(\sigma_h + \sigma_e)$, where $S_{h,e}$ and $\sigma_{h,e}$ represent the Seebeck coefficients and electrical conductivities for the p- and n-type carriers from the hole and electronic bands, respectively [34,35]. It has been pointed out that for materials with a band gap between valence and conduction bands, both S_h and S_e will exhibit the "p-type-like behavior" where the corresponding value increases upon raising the temperature when the Fermi level lies in the valence band [36]. On the other hand, when the Fermi level lies in the conduction band, both S_h and S_e will show the "n-type-like behavior" and the values decrease with increasing temperature.

From the calculated band structure of ScSb, the Fermi energy lies between the valence and conduction bands with small numbers of hole and electron carriers within the

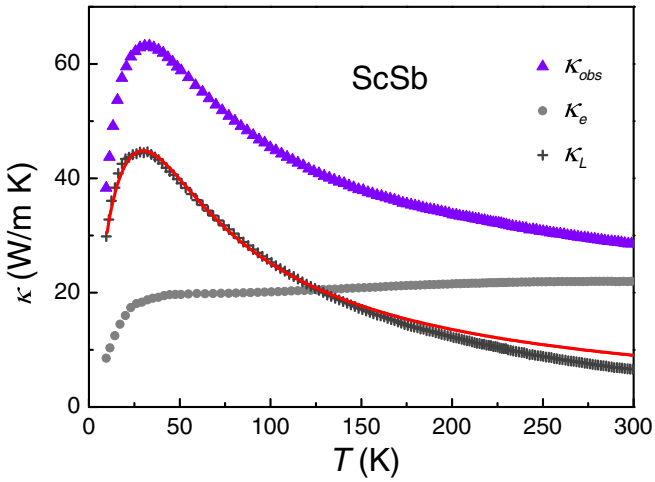

FIG. 3. Temperature variation of the thermal conductivity κ of ScSb. The decomposed electronic and lattice thermal conductivity are presented by circle and cross symbols, respectively. The solid curve represents the fitting result of the lattice thermal conductivity using Eqs. (1) and (2).

corresponding bands. The obtained hole and electron carrier densities are $n_h \approx 7.6 \times 10^{20}$ and $n_e \approx 7.1 \times 10^{20}\,\mathrm{cm}^{-3}$, consistent with the nearly electron-hole compensation with the carrier ratio of 0.93 reported by Hu *et al.* [7]. Thus both electrons and holes intrinsically participate in the thermoelectric transport for the present case of ScSb. The calculated S_h, S_e, and total Seebeck coefficient S_{calc} as a function of temperature are displayed in Fig. 2. Note that both of the contributions from the valence and conduction bands have been taken into account in calculating either S_h or S_e because these bands overlap at around the Fermi level. It thus leads to a competition between the *p*-type-like and *n*-type-like features for both S_h and S_e, giving rising to a nonmonotonic relationship between $S_{h,e}$ and T. At very low temperatures, the electrons smear out to the hole pocket, and both S_h and S_e have the *p*-type-like behavior with the presence of a positive peak feature. On the other hand, the hole pocket is gradually filled with rising temperature, and more electrons are excited to the conduction bands, leading to the *n*-type-like character for both S_h and S_e at high temperatures. Consequently, the sign of S_{calc} is positive at low temperatures and then exhibits a sign reversal upon increasing temperature. The feature of S_{calc} is quite consistent with the temperature variation of S_{expt}, demonstrating that the observed Seebeck coefficient could be qualitatively described by a standard two-band model. It is notable that the entire temperature dependence of S_{expt} in ScSb is very similar to that reported in the isostructural compound of ScAs in spite of a weaker peak feature in the latter analog [37]. The comparison suggests that the mechanisms responsible for the temperature-dependent Seebeck coefficient are similar for both compounds.

Figure 3 illustrates the temperature variation of the thermal conductivity κ measured on a large size of the ScSb crystal (sample 2) with a higher residual resistivity that has little effect on the thermoelectric behavior. Briefly, a peak feature present at around 30 K due to the phonon drag effect is identical with that observed in the Seebeck coefficient. The room-temperature κ of about $28\,\mathrm{W\,m^{-1}\,K^{-1}}$ was found to be much larger than $8\,\mathrm{W\,m^{-1}\,K^{-1}}$ reported in ScAs [37]. In ordinary semimetals such as $Bi_{1-x}Sb_x$ [38], the total thermal conductivity is a sum of electronic and lattice contributions. The electronic thermal conductivity (κ_e) can be evaluated using the Wiedemann-Franz law: $\kappa_e \rho/T = L_0$, where ρ is the dc electrical resistivity and $L_0 = 2.45 \times 10^{-8}\,\mathrm{W\,\Omega\,K^{-2}}$ is the theoretical Lorentz number. The lattice thermal conductivity κ_L is obtained by subtracting κ_e from the observed thermal conductivity $\mathrm{k_{obs}}$. The decomposed κ_e and κ_L are also shown in Fig. 3. It is clear that both κ_e and κ_L contribute to the total thermal conductivity; κ_e dominates at high temperatures while κ_L becomes dominant at low temperatures with a peak feature near 30 K.

To explore the influence of different scattering mechanisms in the thermal transport, κ_L is analyzed by using the Debye-Callaway approximation [39,40]. Accordingly, κ_L can be expressed as

$$\kappa_L = \frac{k_B}{2\pi^2 \upsilon}\left(\frac{k_B T}{\hbar}\right)^3 \int_0^{\Theta_D/T} \frac{x^4 e^x}{\tau_P^{-1}(e^x-1)^2}dx, \qquad (1)$$

where $x = \hbar\omega/k_B T$ is dimensionless, $\hbar$ is the reduced Plank constant, k_B is the Boltzmann constant, ω is the phonon frequency, Θ_D is the Debye temperature, υ is the average phonon velocity, and τ_P^{-1} is the phonon scattering relaxation time. Here τ_P^{-1} is the combination of four scattering mechanisms and is given by

$$\tau_P^{-1} = \frac{\upsilon}{L} + A\omega^4 + B\omega^2 T \exp\left(\frac{-\Theta_D}{3T}\right) + C\omega T^3, \qquad (2)$$

where the grain size L, the Debye temperature Θ_D, and the coefficients A, B, and C are the fitting parameters. The terms in Eq. (2) are the relaxation time for the grain-boundary, point-defect, phonon-phonon umklapp, and phonon-phonon normal scattering, respectively. Here, the sound velocity $\upsilon = 2\pi\Theta_D k_B \frac{[(6\pi^2)/n]^{-1/3}}{h} = 5060\,\mathrm{m/s}$ was used by taking $n = 0.196\,\mathrm{nm}^3$ (the volume of the primitive cell based on the experimental lattice constant $a = 0.5814\,\mathrm{nm}$). It is apparent that κ_L of ScSb can be fitted quite well for $T < 150$ K, drawn as a solid curve in Fig. 3. The fitting parameters $A = 1.35 \times 10^{-43}\,\mathrm{s^3}$, $B = 5.5 \times 10^{-19}\,\mathrm{s/K}$, and $C = 1.92 \times 10^{-11}\,\mathrm{K^{-3}}$ were extracted. Such a fit reveals the Debye temperature $\Theta_D = 260\,\mathrm{K}$ which is close to the value of 275 K derived from the low-temperature specific heat measurement. We also obtained the corresponding grain size L of about 0.29 mm, much larger than that of the polycrystalline specimen and comparable to the actual size of the studied sample.

B. Specific heat measurements

The low-temperature specific heat C_p measured between 1.8 and 10 K is shown in Fig. 4. The temperature dependence of C_p for ScSb exhibits a smooth increase with no sign of the magnetic or superconducting phase transition. For nonmagnetic metals, the specific heat can be expressed as $C_p(T) = \gamma T + \beta T^3$ at low temperatures. The first term is the electronic specific heat associated with the Sommerfeld coefficient γ, while the second term arises from the contribution of the phonons without considering the anharmonic

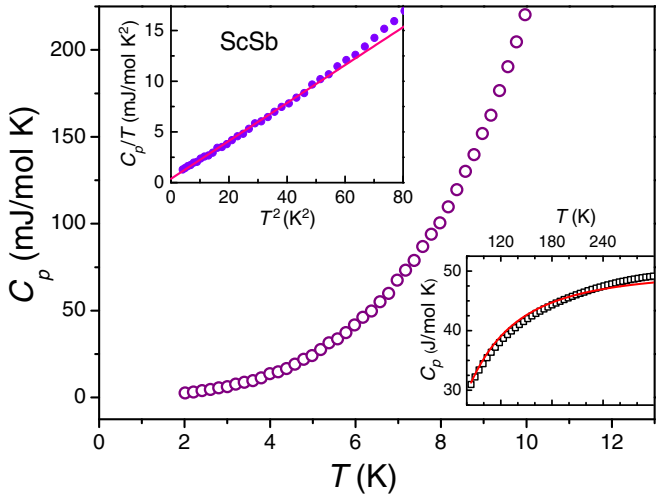

FIG. 4. Temperature dependence of the specific heat C_p of ScSb between 1.8 and 10 K. The upper inset is a plot of C_p/T vs T^2, in which the solid line is a fit to the experimental data according to $C_p/T = \gamma + \beta T^2$ between 1.8 and 7.6 K. The lower inset shows the high-temperature specific heat data with a fitting curve according to Eq. (3).

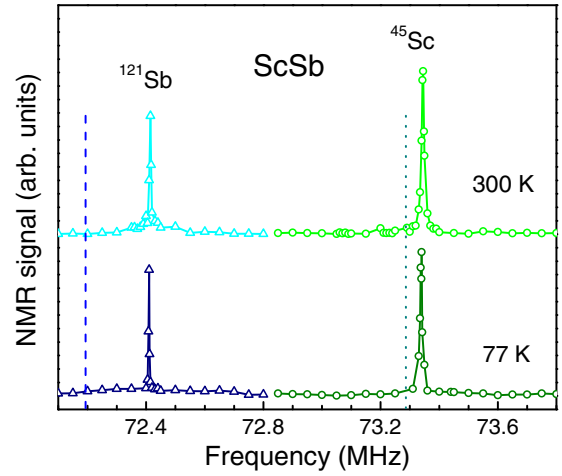

FIG. 5. ^{45}Sc and ^{121}Sb NMR central transition spectra of ScSb measured at 77 and 300 K. The dotted and dashed lines denote the positions of the ^{45}Sc and ^{121}Sb NMR reference frequency, respectively.

effect. In the upper inset of Fig. 4, we plotted C_p/T vs T^2, with a solid line representing the best fit to the experimental data. Such a fit yields the values of $\gamma = 0.38\,\mathrm{mJ\,mol^{-1}\,K^{-2}}$ and $\beta = 0.187\,\mathrm{mJ\,mol^{-1}\,K^{-4}}$. The Debye temperature $\Theta_D = 275\,\mathrm{K}$ was derived from β using $\Theta_D = (12\pi^4 zR/5\beta)^{1/3}$, where $z = 2$ is the number of atoms per formula unit and $R = 8.314\,\mathrm{J\,mol^{-1}\,K^{-1}}$ is the gas constant. The deduced Debye temperature is very close to the theoretical value of 280 K [18]. From the Sommerfeld theory of conduction, the measured γ can be used to estimate the Fermi-level density of states (DOS) $N(\varepsilon_F)$ via $\gamma = (\pi^2/3){k_B}^2 N(\varepsilon_F)$, where k_B is the Boltzmann constant and ε_F is the Fermi energy. Accordingly, a small $N(\varepsilon_F) = 0.16$ states/eV in ScSb was extracted. Such a low $N(\varepsilon_F)$ is consistent with the theoretical results showing a slight overlap between the electron and hole pockets and a pseudogap feature in the vicinity of the Fermi level [7,14,15].

The high-temperature specific heat measured between 85 and 300 K is given in the lower inset of Fig. 4. The data were fitted to the Debye model as

$$C_P(T) = \gamma T + a\left(\frac{T}{\Theta_D}\right)^3 \int_0^{\frac{\Theta_D}{T}} \frac{e^x x^4}{(e^x - 1)^2} dx. \qquad (3)$$

The first term is due to the electronic contribution, while the second term arises from the phonon contribution to the specific heat. Here, the values of $\gamma = 0.38\,\mathrm{mJ\,mol^{-1}\,K^{-2}}$ and $\Theta_D = 275\,\mathrm{K}$ were fixed and the Debye term a was the fitting parameter. We thus deduced $a = 150.1\,\mathrm{J\,mol^{-1}\,K^{-1}}$, in good agreement with the theoretical value of $149.7\,\mathrm{J\,mol^{-1}\,K^{-1}}$. The fitting result, plotted as a solid curve, indicates that the high-temperature specific heat data can be reasonably described by the Debye model.

C. ^{45}Sc and ^{121}Sb NMR measurements

Nuclear magnetic resonance is known as a local probe yielding information about Fermi surface features [41–44]. In Fig. 5, we showed both ^{45}Sc and ^{121}Sb NMR central transition line shapes measured at 77 and 300 K, respectively. The observed lines are very narrow, giving no indication of Sc/Sb antisite disorder. A similar sharp feature in the ^{45}Sc NMR central transition line has been reported in the cubic Heusler compound of $ScAu_2Al$ [45]. In addition, we found no quadrupole splitting effect in ScSb, in agreement with the cubic symmetry of the charge distribution around the neighboring lattice sites. The isostructural compound of YbSb also exhibits the same behavior in the ^{121}Sb NMR central transition line [46]. The ^{45}Sc and ^{121}Sb NMR spectra of ScSb show little change with temperature, consistent with the Pauli-type paramagnetic character. The corresponding Knight shift was determined from the frequency of the maximum ν_o relative to the reference frequency ν_{ref} as denoted by a vertical line. According to the Knight shift $K = (\nu_o - \nu_{\mathrm{ref}})/\nu_o$, we obtained $^{45}K = 0.07\%$ for ^{45}Sc and $^{121}K = 0.3\%$ for ^{121}Sb NMR Knight shifts of ScSb, respectively.

The observed ^{45}K can be expressed as $^{45}K = {}^{45}K_{\mathrm{orb}} + {}^{45}K_s + {}^{45}K_d$. Here $^{45}K_{\mathrm{orb}}$ represents the orbital Knight shift, arising from the orbital magnetic moment of electrons induced by the applied field. $^{45}K_s$ is the s-contact Knight shift due to the s-character electrons around the Fermi level. $^{45}K_d$ is the d-spin shift, which involved the spin polarization of the closed s shells and the s-character electrons in the conduction bands via d electrons. Note that $^{45}K_d$ is negative, owing to the antiparallel orientation between core spins and the unpaired spins responsible for the polarization [47]. Since the determined ^{45}K is positive, it suggests that the contribution from $^{45}K_d$ is overwhelmed by the positive $^{45}K_{\mathrm{orb}}$. While $^{45}K_s$ is also positive, it is less important because of extremely low Fermi-level s DOS from Sc atoms in ScSb. Likewise, ^{121}K can be decomposed as $^{121}K = {}^{121}K_{\mathrm{orb}} + {}^{121}K_s + {}^{121}K_p$. The last term $^{121}K_p$ is connected to the spin polarization from $5p$ electrons, which would make a negative frequency shift. Therefore, the observed positive value of $^{121}K = 0.3\%$ is mainly associated with the s-character and orbital electrons of Sb atoms.

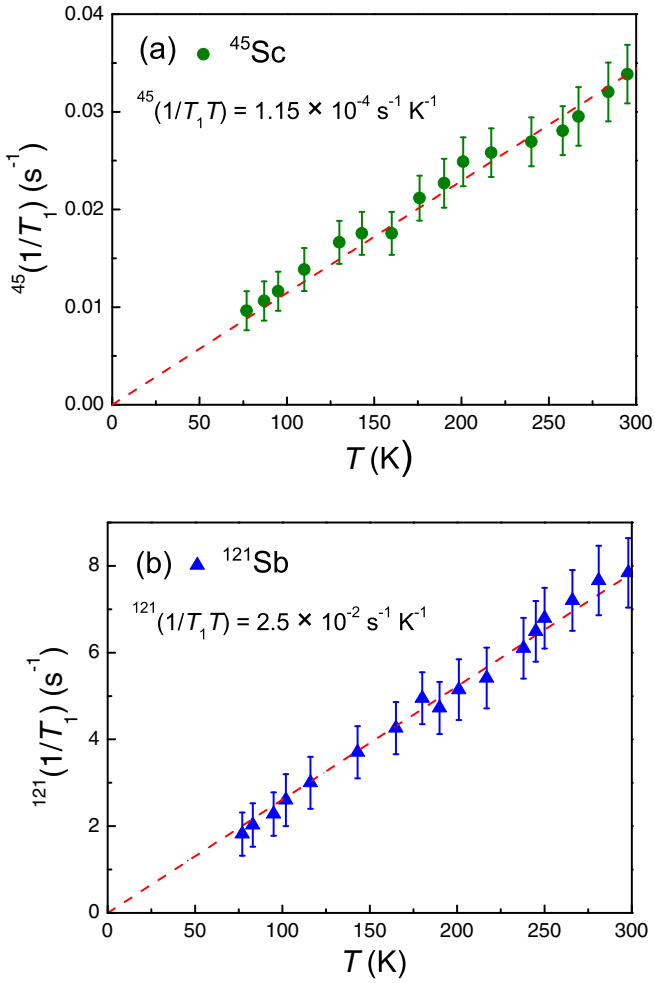

FIG. 6. (a) Temperature dependence of the ^{45}Sc spin-lattice relaxation rate $^{45}(1/T_1)$ of ScSb. (b) Temperature variation of the ^{121}Sb spin-lattice relaxation rate $^{121}(1/T_1)$ of ScSb. Each dashed line indicates the Korringa behavior for the relaxation rates.

Figure 6(a) shows the temperature dependence of the ^{45}Sc spin-lattice relaxation rate $^{45}(1/T_1)$ of ScSb. The observed relaxation rates obey the Korringa behavior, $1/T_1$, proportional to the temperature, as demonstrated by the straight dashed line passing through the data points. Here, two relaxation mechanisms dominate the experimental relaxation rates: $^{45}(1/T_1)_{\rm expt} = {}^{45}(1/T_1)_{\rm orb} + {}^{45}(1/T_1)_d$. The first term arises from the orbital electrons, while the second term is due to the d-spin core polarization. Since the NMR relaxation rate is weakly enhanced by the electron-electron interactions in a nonmagnetic metal, both can be considered to measure the band density of states. Based on the noninteracting picture, each relaxation rate is proportional to the temperature as

$$^{45}\left(\frac{1}{T_1T}\right)_{\rm orb} 2hk_B\left[^{45}\gamma_n H_{hf}^{\rm orb} N_d(\varepsilon_F)\right]^2 p, \tag{4}$$

$$^{45}\left(\frac{1}{T_1T}\right)_{d} 2hk_B\left[^{45}\gamma_n H_{hf}^{d} N_d(\varepsilon_F)\right]^2 q. \tag{5}$$

Here h and k_B are the Planck constant and Boltzmann constant, respectively. $^{45}\gamma_n = 2\pi \times 10.343$ MHz/T is the ^{45}Sc nuclear gyromagnetic ratio; $H_{hf}^{\rm orb}$ is the orbital hyperfine field per unit orbital angular momentum; H_{hf}^{d} is the hyperfine field per electron of the Sc $3d$ electrons; $N_d(\varepsilon_F)$ is the partial Fermi-level d-DOS in units of states/eV spin. The parameters p and q are the reduction factors, which depend on the relative weight of the Fermi level of the irreducible representations of the atomic d functions. Taking $H_{hf}^{\rm orb} \approx 14.8$ T and $H_{hf}^{d} \approx -6.4$ T in Sc-based metals [48,49], $p = 0.4$ in the reduced factor for the equal orbital at the Fermi surface, and $q = 0.2$ for the equal contribution from all five d orbitals, the combination of Eqs. (4) and (5) yields $N_d(\varepsilon_F) \approx 0.04$ states/eV f.u. as using the experimental value of $^{45}(1/T_1T)_{\rm expt} = 1.15 \times 10^{-4}$ s^{-1} K^{-1}. The obtained Fermi-level d-DOS from Sc atoms is rather low, confirming the semimetallic nature for ScSb.

The temperature variation of the ^{121}Sb spin-lattice relaxation rate $^{121}(1/T_1)$ is displayed in Fig. 6(b). For the ^{121}Sb T_1, it is mainly governed by the s-character electrons around the Fermi level due to a large hyperfine field from the $5s$ electrons of the Sb atoms. The contribution from the $5p$ electrons is negligible since the corresponding hyperfine field is about two orders of magnitude lower than that of the $5s$ electrons [47]. In this respect, the relaxation rate expressed as the inverse Korringa relation is

$$^{121}\left(\frac{1}{T_1T}\right)_{s} 2hk_B\left[^{121}\gamma_n H_{hf}^{s} N_s(\varepsilon_F)\right]^2. \tag{6}$$

Here $^{121}\gamma_n = 2\pi \times 10.189$ MHz/T is the ^{121}Sb nuclear gyromagnetic ratio; H_{hf}^{s} is the hyperfine field per electron of the Sb $5s$ electrons; $N_s(\varepsilon_F)$ is the partial Fermi-level s-DOS in units of states/eV spin. From $^{121}(1/T_1T)_{\rm expt} = 2.5 \times 10^{-2}$ s^{-1} K^{-1} and $H_{hf}^{s} \approx 1450$ T [47], a small value of $N_s(\varepsilon_F) \approx 4 \times 10^{-3}$ states/eV f.u. of the Sb $5s$ electrons was thus obtained. Taking the total Fermi-level DOS $N(\varepsilon_F) = 0.16$ states/eV f.u. and partial DOS $N_d(\varepsilon_F) = 0.04$ states/eV f.u. of the Sc $3d$ electrons, we can deduce the partial Fermi-level p-DOS $N_p(\varepsilon_F) \approx 0.12$ states/eV fu of the Sb $5p$ electrons. Such an estimate gives the ratio of $N_p(\varepsilon_F)/N_s(\varepsilon_F) \approx 30$ for Sb atoms in ScSb, consistent with the theoretical calculations which indicate the $5p$ electrons of the Sb atoms are dominant at the Fermi level [7,14,15].

IV. CONCLUSIONS

In summary, we have measured the Seebeck coefficient, thermal conductivity, specific heat, and NMR on single-crystalline ScSb. The observed Seebeck coefficient can be described well by means of a standard two-band model. The Debye model can be employed to analyze the lattice thermal conductivity of ScSb. In particular, small values of the Fermi-level DOS have been extracted from the analyses of the low-temperature specific heat and NMR spin-lattice relaxation rates. In this respect, it allows us to conclude that ScSb is essentially a conventional semimetal in nature.

ACKNOWLEDGMENTS

This work was supported by the Ministry of Science and Technology of Taiwan under Grants No.

MOST-109-2112-M-006-013-MY3 (C.S.L.) and No. MOST-109-2112-M-259-007-MY3 (Y.K.K.). The authors gratefully acknowledge Shu-Yi Sun for the help with performing the NMR spectroscopy measurement at the Core Facility Center of National Cheng Kung University under Grant No. MOST-110-2731-M-006-001.

[1] F. Tafti, Q. Gibson, S. Kushwaha, N. Haldolaarachchige, and R. Cava, Nat. Phys. **12**, 272 (2016).
[2] L.-K. Zeng, R. Lou, D.-S. Wu, Q. N. Xu, P.-J. Guo, L.-Y. Kong, Y.-G. Zhong, J.-Z. Ma, B.-B. Fu, P. Richard, P. Wang, G. T. Liu, L. Lu, Y.B. Huang, C. Fang, S.-S. Sun, Q. Wang, L. Wang, Y.-G. Shi, H. M. Weng *et al.*, Phys. Rev. Lett. **117**, 127204 (2016).
[3] J. F. He, C. F. Zhang, N. J. Ghimire, T. Liang, C. J. Jia, J. Jiang, S. J. Tang, S. D. Chen, Y. He, S. K. Mo, C. C. Hwang, M. Hashimoto, D. H. Lu, B. Moritz, T. P. Devereaux, Y. L. Chen, J. F. Mitchell, and Z.-X. Shen, Phys. Rev. Lett. **117**, 267201 (2016).
[4] J. Xu, N. J. Ghimire, J. S. Jiang, Z. L. Xiao, A. S. Botana, Y. L. Wang, Y. Hao, J. E. Pearson, and W. K. Kwok, Phys. Rev. B **96**, 075159 (2017).
[5] O. Pavlosiuk, M. Kleinert, P. Swatek, D. Kaczorowski, and P. Wisniewski, Sci. Rep. **7**, 12822 (2017).
[6] L. Ye, T. Suzuki, C. R. Wicker, and J. G. Checkelsky, Phys. Rev. B **97**, 081108(R) (2018).
[7] Y. J. Hu, E. I. Paredes Aulestia, K. F. Tse, C. N. Kuo, J. Y. Zhu, C. S. Lue, K. T. Lai, and S. K. Goh, Phys. Rev. B **98**, 035133 (2018).
[8] Y.-Y. Wang, L.-L. Sun, S. Xu, Y. Su, and T.-L. Xia, Phys. Rev. B **98**, 045137 (2018).
[9] A. Vashist, R. K. Gopal, D. Srivastava, M. Karppinen, and Y. Singh, Phys. Rev. B **99**, 245131 (2019).
[10] M. M. Hosen, G. Dhakal, B. Wang, N. Poudel, B. Singh, K. Dimitri, F. Kabir, C. Sims, S. Regmi, W. Neff, A. B. Sarkar, A. Agarwal, D. Murray, F. Weickert, K. Gofryk, O. Pavlosiuk, P. Wiśniewski, D. Kaczorowski, A. Bansil, and M. Neupane, Sci. Rep. **10**, 12961 (2020).
[11] F. F. Tafti, Q. D. Gibson, S. K. Kushwaha, J. W. Krizan, N. Haldolaarachchige, and R. J. Cava, Proc. Natl. Acad. Sci. USA **113**, E3475 (2016).
[12] J. Hayashi, I. Shirotani, K. Hirano, N. Ishimatsu, O. Shimomura, and T. Kikegawa, Solid State Commun. **125**, 543 (2003).
[13] P. Rodriguez-Hernandez and A. Munoz, Int. J. Quant. Chem. **101**, 770 (2005).
[14] A. Tubboune, D. Rached, A. Benzair, N. Sekkal, and A. H. Belbachir, Phys. Status Solidi **243**, 2788 (2006).
[15] A. Maachou, B. Amrani, and M. Driz, Physica B (Amsterdam, Neth.) **388**, 384 (2007).
[16] A. Bouhemadou and R. Khenata, Phys. Lett. A **362**, 476 (2007).
[17] D. Varshney, N. Kaurav, U. Sharma, and R. K. Singh, J. Alloys Compd. **448**, 250 (2008).
[18] M. Teng, H. Fu, J. Feng, W. Liu, and G. Tao, J. Mater. Sci. **47**, 6673 (2012).
[19] M. Narimani and Z. Nourbakhsh, J. Phys. Chem. Solids **145**, 109537 (2020).
[20] M. Narimani and Z. Nourbakhsh, Physica E (Amsterdam, Neth.) **127**, 114518 (2021).
[21] See Supplemental Material at http://link.aps.org/supplemental/10.1103/PhysRevB.104.035135 for (1) the experimental data of the electric resistivity, and (2) the first-principles calculations and band structures of ScSb, which includes Refs. [22–28].
[22] M. S. Hybertsen and S. G. Louie, Phys. Rev. B **34**, 5390 (1986).
[23] C. N. Kuo, H. W. Lee, C.-M. Wei, Y. H. Lin, Y. K. Kuo, and C. S. Lue, Phys. Rev. B **94**, 205116 (2016).
[24] C. W. Tseng, C. N. Kuo, H. W. Lee, K. F. Chen, R. C. Huang, C.-M. Wei, Y. K. Kuo, and C. S. Lue, Phys. Rev. B **96**, 125106 (2017).
[25] H. W. Lee, C. R. Hsing, C. M. Chang, and C. M. Wei, J. Phys.: Condens. Matter **32**, 175501 (2020).
[26] M. Shishkin and G. Kresse, Phys. Rev. B **75**, 235102 (2007).
[27] G. K. H. Madsen and D. J. Singh, Comput. Phys. Commun. **175**, 67 (2006).
[28] V. I. Anisimov, F. Aryasetiawan, and A. I. Lichtenstein, J. Phys.: Condens. Matter **9**, 767 (1997).
[29] Y. K. Kuo, B. Ramachandran, and C. S. Lue, Front. Chem. **91**, 165141 (2014).
[30] J. P. Perdew, K. Burke, and M. Ernzerhof, Phys. Rev. Lett. **77**, 3865 (1996).
[31] P. E. Blöchl, Phys. Rev. B **50**, 17953 (1994).
[32] G. Kresse and D. Joubert, Phys. Rev. B **59**, 1758 (1999).
[33] G. Kresse and J. Furthmuller, Phys. Rev. B **54**, 11169 (1996).
[34] Z. M. Gibbs, H.-S. Kim, H. Wang, and G. J. Snyder, Appl. Phys. Lett. **106**, 022112 (2015).
[35] T. C. Chasapis, D. Koumoulis, B. Leung, N. P. Calta, S.-H. Lo, V. P. Dravid, L.-S. Bouchard, and M. G. Kanatzidis, APL Mater. **3**, 083601 (2015).
[36] R. Liu, Y. Ge, D. Wang, and Z. Shuai, CCS Chem. **3**, 1477 (2021).
[37] B. Saparov, J. Mitchell, and A. S. Sefat, Supercond. Sci. Technol. **25**, 084016 (2012).
[38] A. Nikolaeva, L. Konopko, I. Gherghishan, K. Rogacki, P. Stachowiak, A. Jezowski, V. Shepelevichc, V. Prokoshin, and S. Gusakova, Semiconductors **53**, 657 (2019).
[39] J. Callaway, Phys. Rev. **113**, 1046 (1959).
[40] J. Callaway and H. C. von Baeyer, Phys. Rev. **120**, 1149 (1960).
[41] C. S. Lue, S. Chepin, J. Chepin, and J. H. Ross, Jr., Phys. Rev. B **57**, 7010 (1998).
[42] C. S. Lue, T. H. Su, B. X. Xie, and C. Cheng, Phys. Rev. B **74**, 094101 (2006).
[43] S. C. Chen and C. S. Lue, Phys. Rev. B **81**, 075113 (2010).
[44] C. N. Kuo, C. W. Tseng, C. M. Wang, C. Y. Wang, Y. R. Chen, L. M. Wang, C. F. Lin, K. K. Wu, Y. K. Kuo, and C. S. Lue, Phys. Rev. B **91**, 165141 (2015).
[45] C. Benndorf, O. Niehaus, H. Eckert, and O. Janka, Z. Anorg. Allg. Chem. **641**, 168 (2015).
[46] A. Yamamoto, J. Takeda, T. Koyama, T. Mito, S. Wada, I. Shirotani, and C. Sekine, Phys. Rev. B **70**, 220402(R) (2004).
[47] *Metallic Shifts in NMR*, edited by G. C. Carter, L. H. Bennett, and D. J. Kahan (Pergamon, Oxford, 1977).
[48] B. Perrin, P. Descouts, A. Dupanloup, and D. Seipler, J. Phys. F: Met. Phys. **9**, 673 (1979).
[49] C. S. Lue, R. F. Liu, Y. F. Fu, C. Cheng, and H. D. Yang, Phys. Rev. B **77**, 115130 (2008).